Coherent Control of Relativistic Electron Dynamics in Plasma Nanophotonics - Supplementary Information

Ankit Dulat,[1] Sk Rakeeb,[1] Sagar Dam,[1] Amit D. Lad,[1] Yash M. Ved,[1] Sergey Kruk,[2] and G. Ravindra Kumar[1]

[1)] *Tata Institute of Fundamental Research, 1 Homi Bhabha Road, Colaba, Mumbai 400005, India*

[2)] *Nonlinear Physics Centre, Research School of Physics, Australian National University, Canberra ACT 2601, Australia*

(Dated: 4 February 2024)

Summary of contents

S1. Experimental setup for measurement of the angular distribution and energy spectrum of electrons

The angular distributions of electrons were measured with imaging plates (IPs) (FUJI Film, BAS-SR 2025) placed in a cylindrical geometry surrounding the target, covering the angular range from 0 to 360 degrees (see Fig. S1a). The IPs were covered with 110-micron-thick aluminum filter. Distance of IP from the target was 15 cm (i.e., the radius of the cylindrical IP). The energies of fast electrons were measured using electron spectrometers (ESM) (Fig. S1b). Each spectrometer has a 0.1 Tesla magnetic field and an IP as the detector. The measurable range of energies in these spectrometers is 0.1–7.0 MeV.

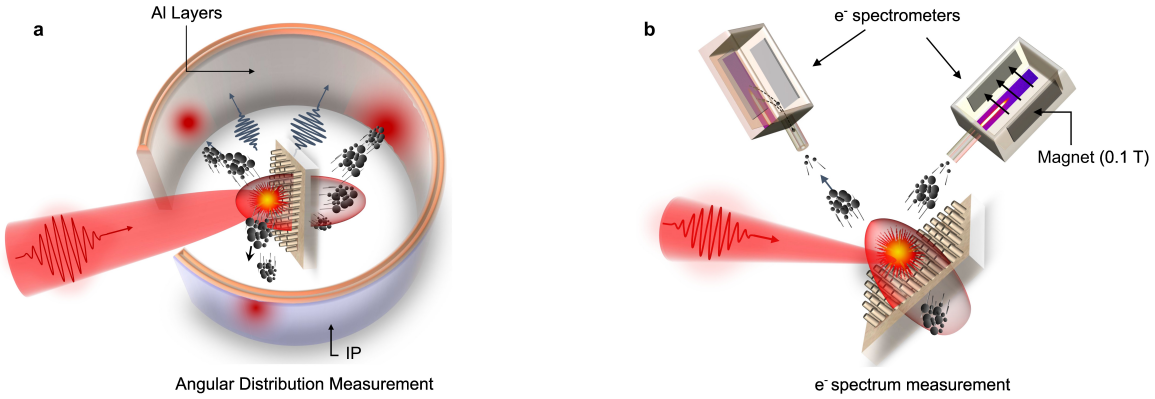

FIG. S1. **Experimental Setup a** Experimental setup to measure the angular distribution of electrons with energy above 100 keV. **b** Setup for measuring the energy spectrum of electrons. Note: In the schematic, both electron spectrometers are shown on the frontside of the target; however, they were placed at angles as specified in the text.

S2. Experimentally measured femtosecond profile and picosecond contrast of the laser pulse

The experimentally measured femtosecond temporal profile of the pulse is shown in Fig. S2a. and the picosecond contrast of the pump pulse is shown in Fig. S2b. The intensity contrast at 25 ps before the peak of the pulse is $\sim 10^{-7}$. To ensure almost insignificant preplasma on the nanopillars, we performed experiments with lower-energy (80 mJ) pulses, corresponding to a peak intensity of 3×10^{18} W/cm^2, which resulted in a very small preplasma of around 50 nm.[1].

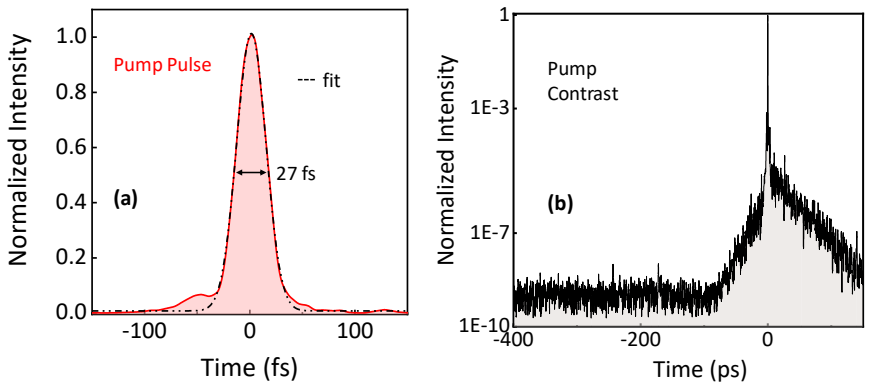

FIG. S2. **The temporal profile of pump pulse characterized using SPIDER[2] and SEQUOIA[3,4].** **a** Shows the femtosecond temporal profile of the pulse. **b** The picosecond contrast of the pulse.

S3. Microscopy images of laser shots on nanostructured target

We fabricated nanopillars on square-shaped regions (islands), with each around 200 μm in size, much larger than the focal spot of our laser pulse ($\sim 8\mu$m). Multiple such small islands of nanostructures were fabricated on a 500 μm-thick fused silica glass substrate. In the experimental vacuum chamber, to spatially overlap the laser spot with the nanostructured islands, we used an auxiliary laser beam, tracing the same path as the main laser pulse. In Fig. S3a, we show some images of the laser-induced damage to the nanostructured target. The green square is the region with the nanopillars, while the transparent region is the glass substrate.

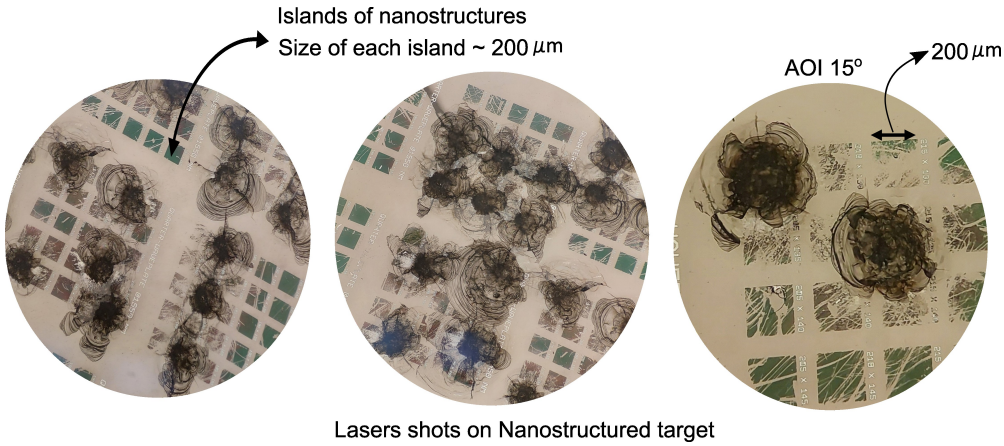

FIG. S3. Microscopy images of laser-induced ablation on the nanostructured target.

S4. Experimentally measured raw angular distribution data for nanostructured targets

In Fig. S4, we present the experimentally measured rear-side raw angular distribution data of electrons ejected from the nanostructured target for different angles of incidence (AOIs) of the pump pulse. Panels a and b compare the angular distribution of electrons measured for an AOI of 15° in two independent experiments. We observe the steering of the electron beam along the direction of 240° in both measurements, but the fraction of electrons deflected varies. In panel, **a**, a significant fraction of electrons remain in the direction normal to the target and the J×B direction. We observe that this behavior depends critically on the alignment of the laser shot on the island of nanopillars shown in Fig. S3. A well-spatially aligned laser shot shows steering for large fractions of electrons which agrees well with the simulations. Panels d and e show similar rear-side angular distributions for an AOI of 40°.

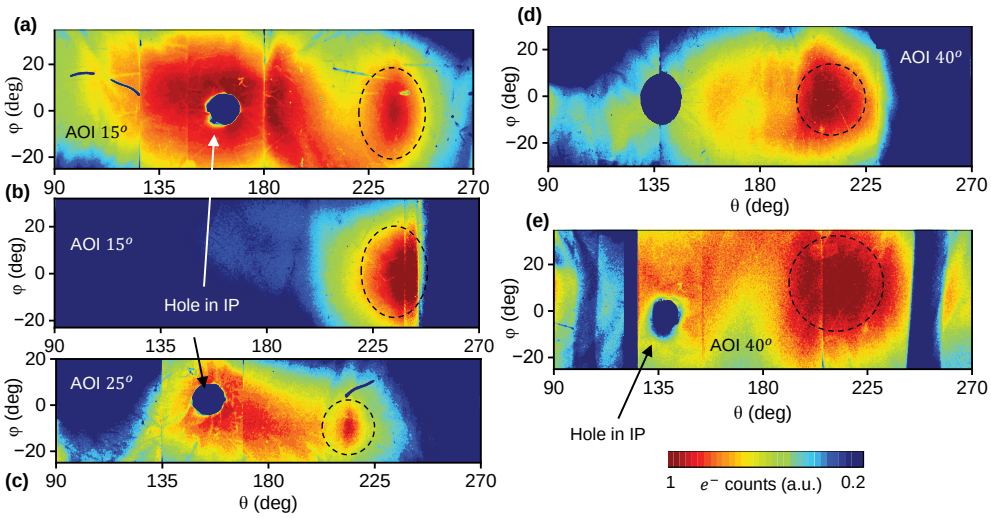

FIG. S4. Experimentally measured rear-side raw angular distribution data of electrons ejected from the nanostructured target for different angles of incidence (AOIs) of the pump pulse.

S5. Experimentally measured raw angular distribution data for a flat target

In Fig. S5, we show the experimentally measured rear-side raw angular distribution data of electrons ejected from the flat target (500 μm thick fused silica glass) for AOIs of 15°, 25°, and 40°, respectively. We observed an electron beam with large divergence along the target normal and the J×B direction.

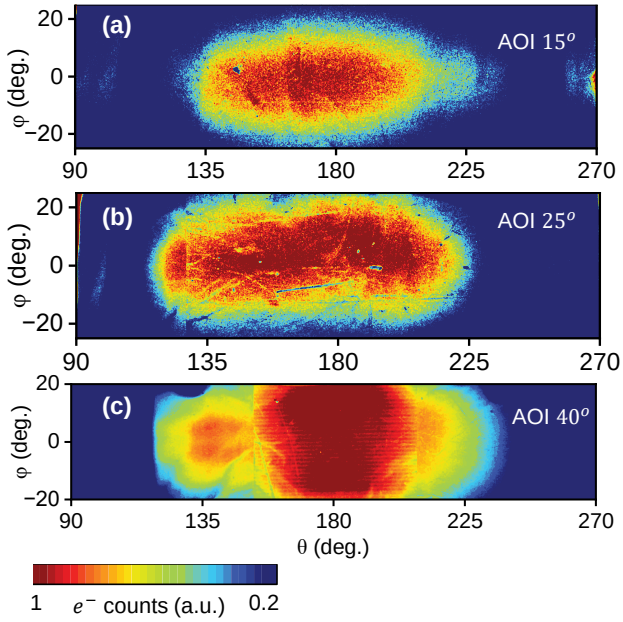

FIG. S5. Experimentally measured rear-side raw angular distribution data of electrons ejected from the flat target for AOIs of 15°, 25°, and 40°, respectively

S6. Experimentally measured raw ESM traces for flat and nanostructured targets

The energy of electrons was measured using the electron spectrometer, as shown in Fig. S1b. The raw data obtained is shown in Fig. S6, which compares the electron energy from flat and nanostructured targets. Each trace was obtained by integrating the electron flux over 15 laser shots. The measurable energy range of the spectrometer is 0.1–7 MeV.

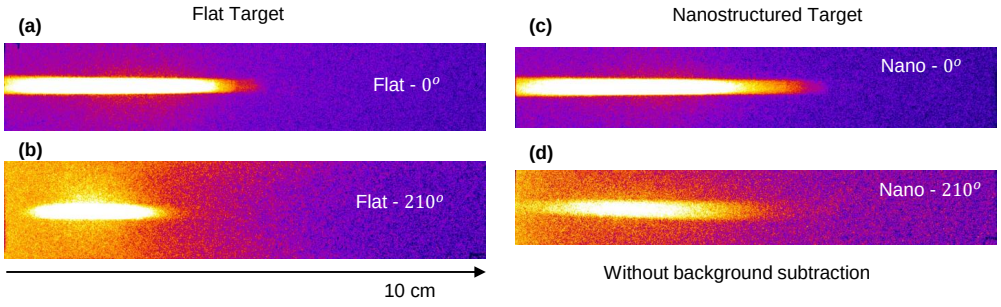

FIG. S6. Measured raw trace of the electron energy spectrum for an AOI of 40°. **(a,c)** shows the ESM trace of electrons along the target front normal, and **(c,d)** shows rear electrons along the guiding direction (210°) for flat and nanostructured targets, respectively.

S7. Comparison of laser energy absorption in nanostructured and flat targets

In Fig. S7, we show the fraction of the laser energy coupled to electrons and ions for both nanostructured and flat targets respectively. We observe, that a large fraction ($\sim 65\%$) of incident laser energy is absorbed by the nanostructured target in comparison to the flat target, where only $\sim 10\%$ laser energy is coupled to the target. In Fig. S7, the red curves show the energy in the field, and the orange curve represents the energy gained by electrons from the initial energy of 100 eV. The curve in green shows the energy gained by ions inside the plasma. We observe that for nanostructured targets, a large fraction of the absorbed laser energy is coupled to electrons, which slowly transfer their energy to ions at a later delay of more than 60 fs.

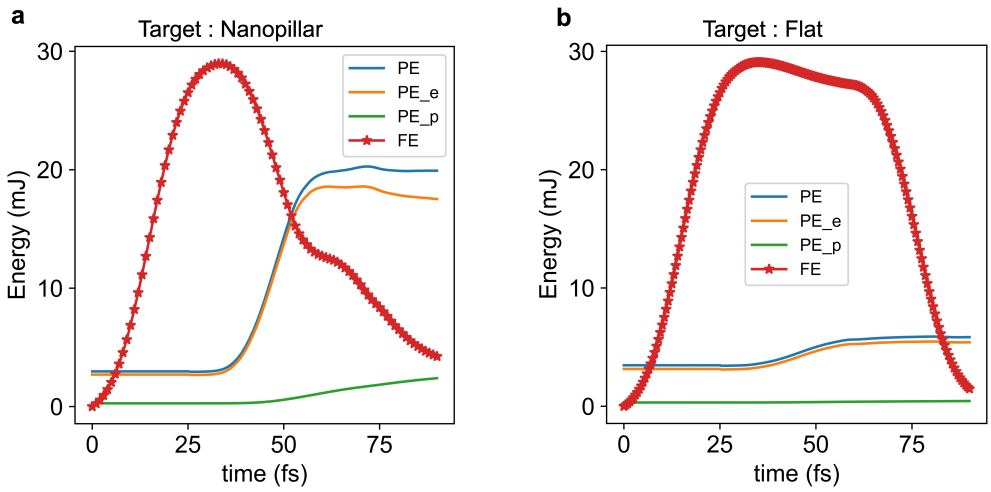

FIG. S7. **2D-PIC simulation results (a,b)** Compares the laser energy coupled to electrons and ions for nanostructured and flat targets respectively.

S8. Electron dynamics inside a single nanopillar of the array

In Fig. S8, we show the electron dynamics near the peak of the laser pulse, inside the central nanopillar of the array. (**b**) present the angular distribution of electrons inside the nanopillar. 0° represents normal to the target, and ±90° is along the target surface. We observe that a fraction of electrons are launched normally to the tip of the nanopillar, while others are injected from the sides (from the gap between the nanopillars). (**d**) shows the energy spectrum of electrons, showing cutoff energy as large as 1.2 MeV. (**e**) shows the phase

space x-p_x of electrons moving along the normal to the target (i.e., along the length of the nanopillar).

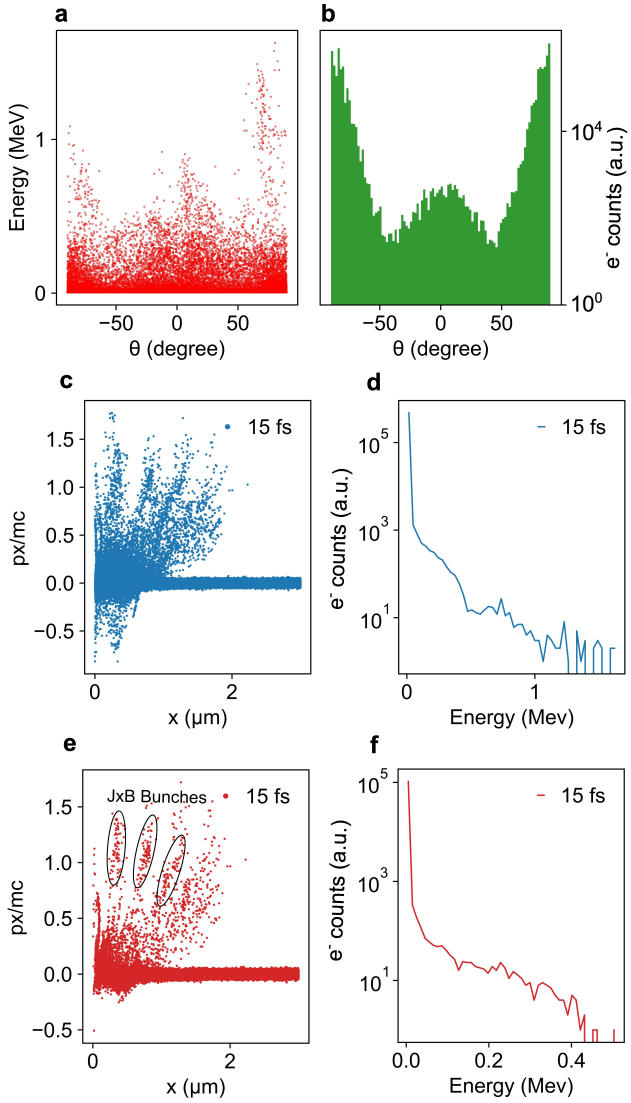

FIG. S8. **Electron dynamics inside single nanopillar a** Energy distribution of electrons moving along different directions inside the nanopillar. **b** Angular distribution of electrons with a lower energy cutoff of 100 keV. **c** Phase space x-p_x of all electrons inside the nanopillar. **d** Energy spectrum of electrons during the peak of the laser pulse. **e** Phase space x-p_x of electrons moving along the normal to the target (i.e. along the length of nanopillar). **f** Energy spectrum of electron moving normal to the tip of nanipillar.

We observe electron bunches launched at twice the laser frequency, a signature of JxB heating. In **f**, we show the energy spectrum of the electrons in (**e**), which shows a maximum

cutoff energy of 400 keV, which is in excellent agreement with the theoretical value of 410 keV, the cutoff energy due to pondermotive/JxB heating.

S9. Effect of changes in the parameters of the nanostructured target on the guiding and acceleration of electron bunches

To better understand the electron dynamics, we performed simulations with varying parameters of the nanopillars in the nanostructured target. We varied mainly two parameters: one is the height (h) of the nanopillar, and the other is its periodicity (d) in the array.

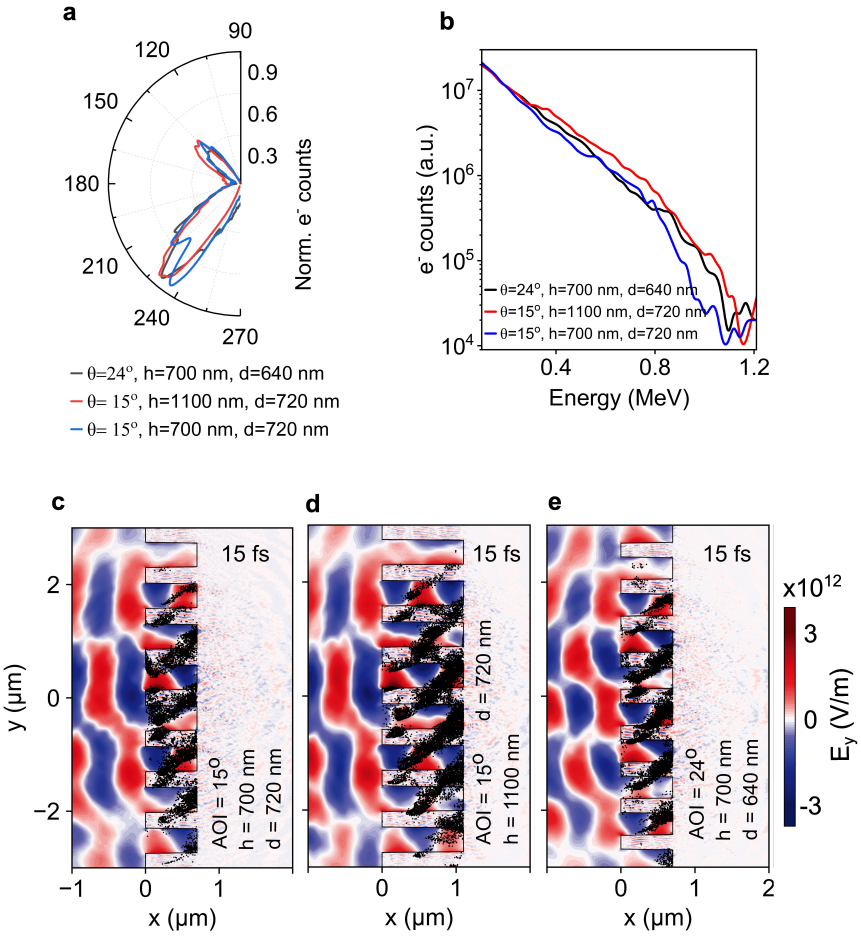

FIG. S9. **a** Rear side angular distribution of electrons for two AOI of the laser pulse and different parameters of nanopillars as labeled. **b** Energy spectrum of rear electrons for the laser and target parameters as labeled. **c,d,e** shows the y component of the electric field (E_y) and the trajectories of electrons with energy greater than 100 keV, for different laser and target parameters as labeled.

In Fig. S9, we plot the rear angular distribution **a**, energy spectrum **b**, and in **c,d,e** the

y-component of the electric field (color plot) with the trajectories of electrons shown by the black scatter plot for different parameters of nanopillars and the AOI of the incident laser pulse. Let us first see the effect of the change in h. We increased h from 700 nm to 1100 nm. For an AOI of 15° in **a**, we plot the angular distribution of electrons for these two different values of h, as shown in the blue and red curves, respectively. We observe that there is no change, neither in the electron flux nor in the directions of emitted electrons. In **b**, we also plot their energy spectrum, which also looks almost identical. To explain this observation, we show the field profile in the near field region in **c,d**, respectively. As shown, not only the field arrangement is the same, but also the trajectories of the electrons look identical in these two cases. It shows that the height of the nanopillar doesn't make any difference in the guiding and acceleration schemes.

To demonstrate the accuracy of our model of steering and acceleration and simultaneously to show the effect of periodicity, we changed the period of the nanopillars from 720 nm to 640 nm. The angle of light diffraction mode on the rear can be calculated using the following formula:

$$\theta_d = \sin^{-1}(\sin\theta_i \pm n\lambda/d) \tag{1}$$

Using eq. (1), we calculate the diffraction angle $\theta_d = 58.3°$ (away from normal) for an AOI of 15° and d = 720 nm. As shown in **a**, this is exactly the direction along which electrons are guided. Now, with the change in the periodicity, i.e., with d = 640 nm, we chose an AOI of 24°. Using eq. (1), we predicted the electron beam to be still in the same direction, i.e., $\theta_d \sim 58°$. As shown in **a**, in the black curve, not only electrons are guided exactly in the same direction, but as shown in **b**, their cutoff energy is also the same, and the corresponding near-field profile and electron trajectories are shown in **e**. This shows the effectiveness of the simple model, i.e., by simply changing either the period of the nanopillars or the AOI of the laser pulses, the spatiotemporal properties of the electron beam can be controlled very easily.

S10. Comparison of electron bunching dynamics, phase space, and energy spectrum for different AOIs

In Fig. S10, we show the trajectories of electrons on the rear side of the nanostructured target, their phase space r-p_x, and the energy spectrum of electrons for three different AOIs

of 15°, 25°, and 40°, respectively. We plot three horizontal panels, each with a different AOI of the laser pulse. Each panel has three figures. For an AOI of 15°, **a** show the trajectories of electrons on the rear side of the nanostructured target plotted at two different times of 30 fs and 35 fs. We observe the electrons in a "wavefront"-like arrangement with a period of 2.5 fs. In **b**, we show the phase space r-p_x, where $\hat{r}$ is the direction along which the electrons are guided. **c** shows the energy spectrum of electrons on the rear. Similarly, the second and third panels compare it for two other different AOIs of 25° and 40°, respectively, as labeled.

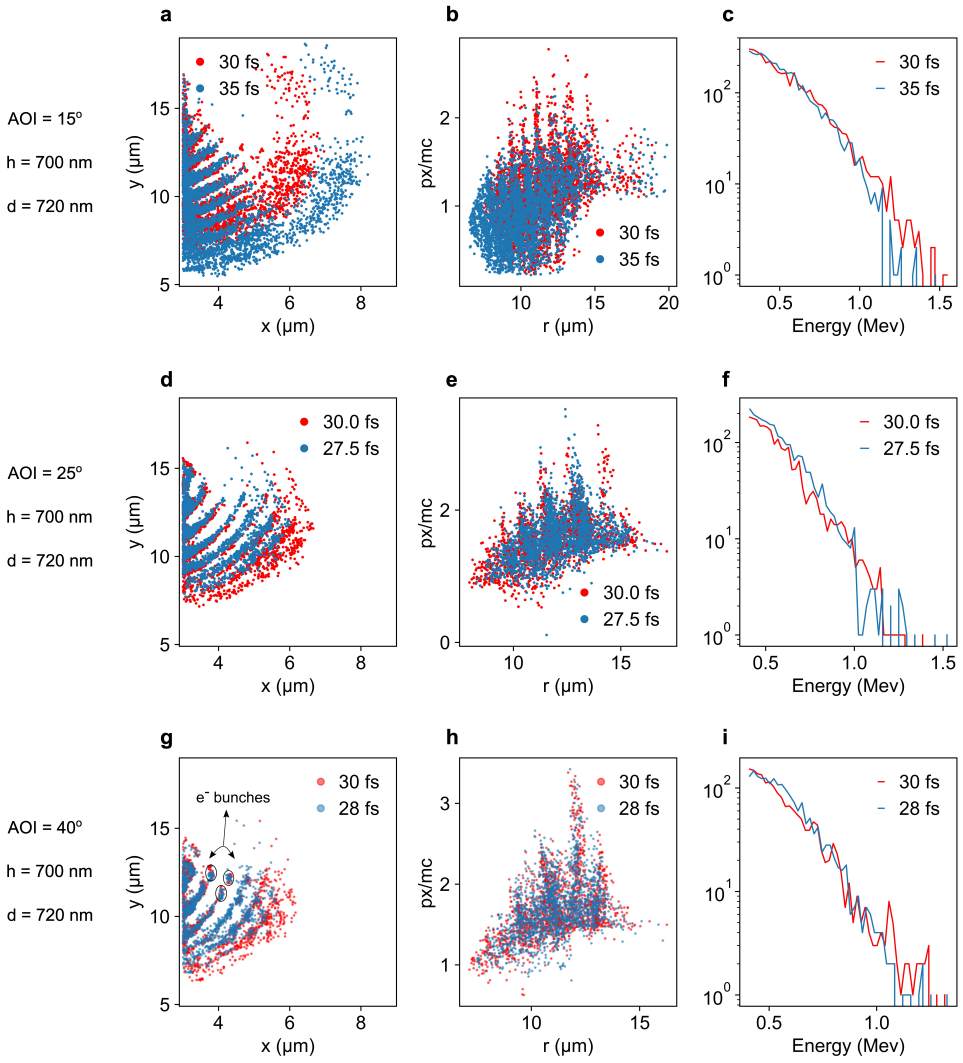

FIG. S10. For three different AOIs of 15°, 25°, and 40° (**a,d,g**), compare the trajectories of rear-side electrons for two different time delays. (**b,e,h**) compares the phase-space r-p_x of rear electrons. (**c,f,i**) compares the energy spectrum of rear-side electrons.

S11. Current and density profile in the nanostructured target

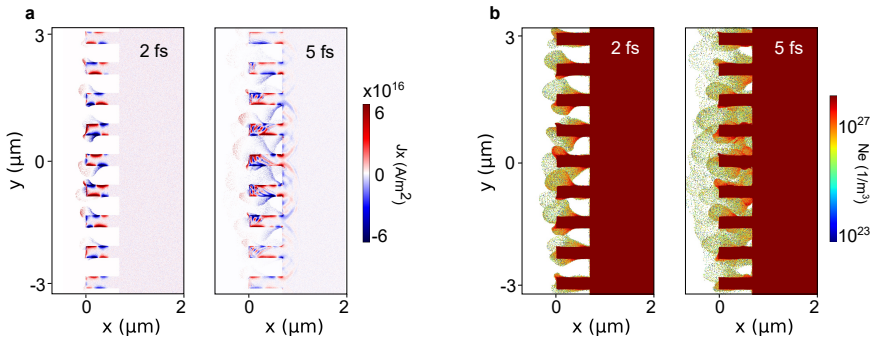

FIG. S11. **a** The x-component of current density (J_x) at 2 and 5 fs after the interaction of the laser pulse. **b** Number density of electrons as ionized by the laser field at 2 and 5 fs time delays.

S12. References

[1]A. Dulat, C. Aparajit, A. Choudhary, A. D. Lad, Y. M. Ved, B. S. Paradkar, and G. R. Kumar, "Sub-picosecond pre-plasma dynamics of a high contrast, ultraintense laser–solid target interaction," Opt. Lett. **47**, 5684–5687 (2022).

[2]C. Iaconis and I. A. Walmsley, "Spectral phase interferometry for direct electric-field reconstruction of ultrashort optical pulses," Opt. Lett. **23**, 792–794 (1998).

[3]G. Albrecht, A. Antonetti, and G. Mourou, "Temporal shape analysis of Nd^{3+}: YAG active passive model-locked pulses," Optics Communications **40**, 59 – 62 (1981).

[4]R. C. Eckardt and C. H. Lee, "Optical third harmonic measurements of subpicosecond light pulses," Applied Physics Letters **15**, 425–427 (1969).